JGR Space Physics

Key Points:
- Electromagnetic ion cyclotron wave spectra are most consistent with low helium and oxygen fractions
- Radiation belt simulations are most sensitive to the cold ion helium fraction
- Stronger agreement with observations is found using ion compositions with low helium fractions

Correspondence to:
J. P. J. Ross,
johros@bas.ac.uk

The Importance of Ion Composition for Radiation Belt Modeling

J. P. J. Ross[1] [ID], **S. A. Glauert[1]** [ID], **R. B. Horne[1]** [ID], and **N. P. Meredith[1]** [ID]

[1]British Antarctic Survey, Natural Environment Research Council, Cambridge, UK

Abstract The banded structure of electromagnetic ion cyclotron (EMIC) wave spectra and their resonant interactions with radiation belt electrons depend on the cold ion composition. However, there is a great deal of uncertainty in the composition in the inner magnetosphere due to difficulties in direct flux measurements. Here, we show that the hydrogen and helium band wave spectra are most consistent with a helium and oxygen composition of a few percent. Less than 10% of hydrogen band wave intensity is consistent with a high helium fraction of ~20%. Similarly, only ~20% helium band wave intensity is consistent with an oxygen torus ion composition. Furthermore, we find that the decay of the ultra-relativistic electrons in the radiation belts by EMIC waves depends on the ion composition. The decay is most sensitive to the helium fraction, and the strongest agreement with Van Allen Probes data is found when the helium fraction is a few percent. We suggest that more observations of the cold ion composition would significantly help understand and set constraints on the decay of ultrarelativistic electrons in the radiation belts.

Plain Language Summary The radiation belts are rings of charged particles around the Earth that are largely confined by the Earth's magnetic field. Electromagnetic waves can interact with these particles, leading to acceleration, transport, and loss. In the outer belt, electrons can be rapidly accelerated during geomagnetic storms leading to a large population of ultrarelativistic electrons. Electromagnetic ion cyclotron waves are particularly important for the decay of this ultrarelativistic population, as they are effective at scattering these electrons into the atmosphere, removing them from the belts. In this work, we show that the cold ion composition is important in determining the rate of decay of these electrons and find that the strongest agreement between models and observations when the He^+ fraction is only a few percent.

1. Introduction

Electromagnetic ion cyclotron (EMIC) waves are important for the losses of relativistic electrons in the radiation belts by resonant wave-particle interactions (Thorne & Kennel, 1971). Doppler-shifted cyclotron resonance between EMIC waves and relativistic radiation belt electrons can lead to pitch-angle diffusion of the electrons and consequently losses from the belts. These interactions are believed to be responsible for several observational phenomena such as precipitating relativistic electrons (Miyoshi et al., 2008; Rodger et al., 2008; Usanova et al., 2014; Yuan et al., 2018), the narrowing of pitch-angle distributions and decay of the ultrarelativistic electrons (Drozdov et al., 2017; Kersten et al., 2014; Ross et al., 2020; Shprits et al., 2016; Usanova et al., 2014) and deepening local minima in phase space density (Shprits et al., 2017).

The resonant interactions between waves and radiation belt electrons are dependent on the wave and plasma properties. EMIC waves are no exception. For instance, high-density regions and wave-frequencies close to the upper bounding gyrofrequency lead to interactions at lower electron energies and higher pitch-angles (Meredith et al., 2003; Summers & Thorne, 2003). Watt et al. (2019) showed that including the variation in these parameters is important for capturing the effects of hiss waves on radiation belt electrons. Observations of these parameters are readily available for EMIC waves at $L \geq 3.0$ thanks to high-frequency magnetometer satellite observations and wave measurements, and have been included in electron diffusion models (Ross et al., 2020, 2021). However, the ion composition of the cold plasma also significantly affects the resonant interactions (Meredith et al., 2003) and the banded structure of EMIC waves (Lee et al., 2021). In particular, high ion fractions of the ion species of the EMIC wave band favor lower resonant energies (Albert, 2003; Summers & Thorne, 2003), while an increased fraction of heavier ions can restrict the frequency range. Direct observations of cold ions are difficult due to spacecraft charging (Olsen et al., 1985) resulting in significant uncertainty.

Table 1
Ion Compositions

References	Abbreviation	η_{H+}	η_{He+}	η_{O+}	$I_{stop}^{H+}/I(\%)$	$I_{stop}^{He+}/I(\%)$
Kersten et al. (2014)	K14	0.94	0.05	0.01	93.6	98.8
Meredith et al. (2003)	M03	0.70	0.20	0.10	8.4	77.6
Nosé et al. (2020)	N20	0.806	0.034	0.16	83.5	22.6

The ion composition depends on magnetic activity (Young et al., 1982), magnetic local time (Lee & Angelopoulos, 2014), and radial distance from the Earth. For instance, a region of enhanced O⁺, known as the oxygen torus, forms during the storm recovery phase (Chappell, 1988; Comfort et al., 1988; Horwitz, 1984). Multiple methods have been used to determine the cold ion composition in the magnetosphere using both remote sensing and in situ means (see André and Cully (2012) for a review and references therein). The ion compositions reported varying significantly between such studies. As a result, a wide range of values have been adopted for radiation belt modeling, such as storm main phase estimates of 70% hydrogen, 20% helium, and 10% oxygen (Drozdov et al., 2017; Ma et al., 2015; Meredith et al., 2003; Shprits et al., 2016; Usanova et al., 2014) to 94% hydrogen, 5% helium, and 1% oxygen estimated from EMIC crossover frequencies (Kersten et al., 2014). Since the ion composition plays an important role in setting the minimum resonant energy, the frequency bandwidth (Denton et al., 2015), and the dominant polarisation of the waves (left and right), changes in the ion composition should play an important role in radiation belt physics. The purpose of this paper is to investigate how the ion composition affects the dynamics of the high-energy electron flux using global simulations.

2. Minimum Resonant Energies

To test the importance of ion composition, we consider three ion compositions that are given in Table 1. K14 is an average composition estimated based on the crossover frequency from Kersten et al. (2014) and has notably low η_{He+} and η_{O+}. M03 is a storm time estimate from Meredith et al. (2003) which has significantly higher heavy ion fractions. Finally, N20 is from an observation of the oxygen torus and therefore has a high oxygen fraction (Nosé et al., 2020).

The minimum resonant energy, E_{min}, between a parallel propagating EMIC wave ($\psi = 0°$ where ψ is the wave normal angle) and an electron can be calculated by equation 6 from Summers and Thorne (2003) which assumes a cold plasma, composed of electrons, hydrogen ions, helium ions, and oxygen ions. We denote the ion fraction of species i with η_i. In addition to the ion composition, E_{min} depends on the ratio of the wave frequency to proton gyrofrequency, f/f_{cp}, and the plasma frequency to electron gyrofrequency ratio, f_{pe}/f_{ce}. For illustration, for both hydrogen and helium band EMIC waves, we adopted the 80th percentile for the EMIC wave frequency to proton gyrofrequency ratio from Ross et al. (2021) because the high-frequency EMIC waves have the most significant contribution to radiation belt electrons with energies of several MeV.

Figure 1. Panel (a) shows the dispersion curves for a parallel propagating wave with $f_{pe}/f_{ce} = 20$. The green, red, and orange lines correspond to the ion compositions M03, N20, and K14. The solid and dotted lines correspond to the left-handed and right-handed waves. Panels (b)–(d) show E_{min} as a function of ion composition for different values of f/f_{cp} and f_{pe}/f_{ce}. For (b) and (d), $f/f_{cp} = 0.19$, and for (c) and (e), $f/f_{cp} = 0.45$. For (b) and (c), $f_{pe}/f_{ce} = 10$, and for (d) and (e), $f_{pe}/f_{ce} = 20$. Contours in E_{min} every 1 MeV up to 20 MeV are indicated by the black dotted lines, with the exception of the 2 MeV line shown in white. Note that the 2 MeV line is only visible in panels (d) and (e) as it falls within the displayed composition range. Lines of fixed η_{He+} (b) and (d) and η_{H+} (c) and (e) are indicated by the red dotted lines. The red pluses, orange triangles, and green squares correspond to the ion compositions in N20, K14, and M03, respectively.

The effect of ion composition on the EMIC dispersion curves is shown in Figure 1a, where the wave number is given by k. The N20 ion composition (red) has the largest stop band for helium band EMIC waves, restricting the permissible frequencies closer to the helium gyrofrequency than for M03 and K14. While for hydrogen band waves, M03 (green) has the largest stop band. More generally, if we consider the heavy ion dependence for a helium band wave with fixed f/f_{cp} ($f/f_{cp} = 0.19$) and $f_{pe}/f_{ce} = 10$ (Figure 1b) and $f_{pe}/f_{ce} = 20$ (Figure 1d), when either the helium or oxygen fraction is increased, the stop
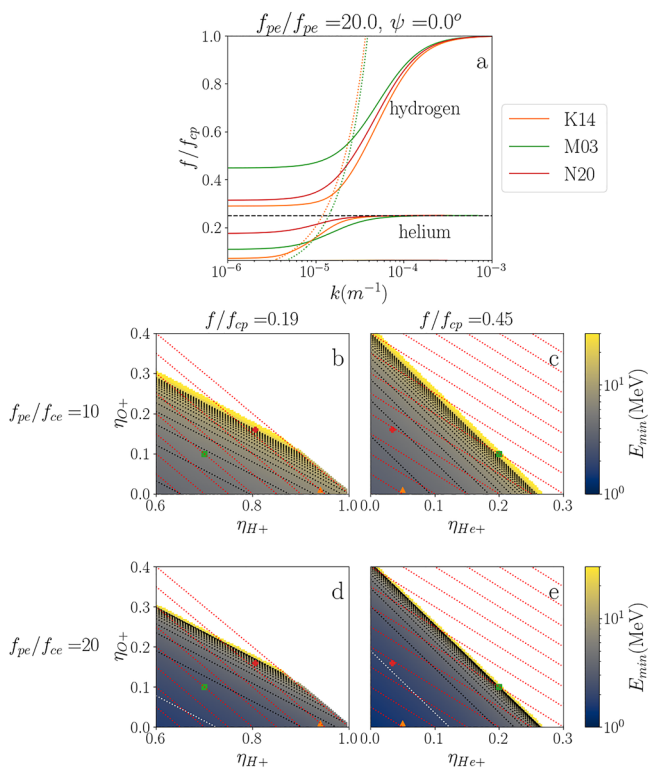
band will eventually exceed f/f_{cp} and therefore no parallel propagating helium band EMIC wave can exist, as indicated by the white region. When (η_{He+}, η_{O+}) approaches the threshold from low η_{H+} and low η_{O+}, $E_{\min}$ increases, that is, moving from the lower left corner of Figure 1b toward the threshold. As the threshold is approached, the minimum resonant energy increases, which corresponds to resonances at lower wave numbers.

Figures 1b–1e also show the sensitivity to the helium fraction which we discuss later. For helium band EMIC waves, $E_{\min}$, which is given by the color in Figure 1, with N20 (red plus sign) is much higher than for the other compositions for both values of f_{pe}/f_{ce}. The resonant energy for the helium band wave is lowest for the storm time ion composition M03 (green square) owing to the high helium fraction. For hydrogen band waves, the minimum resonant energy is highest for M03 and lowest for K14 due to the high hydrogen fraction (orange triangles). Therefore, the ion composition choice will significantly change $E_{\min}$.

Cao et al. (2017) showed that in a hot plasma, $E_{\min}$ only drops significantly below 2 MeV if the oxygen fraction is small and the electron number density is higher than typical plasmaspheric densities. Our cold plasma results are generally consistent with their results, with $E_{\min} < 2$ MeV only for our higher density case ($f_{pe}/f_{ce} = 20$) and $\eta_{O+} < 0.08$ for helium band EMIC waves and $\eta_{O+} < 0.2$ for hydrogen band EMIC waves. It is worth noting that Ross et al. (2021) found that helium band EMIC waves typically occur in significantly higher density regions than average plasmaspheric values at $L^* > 4.5$. Therefore, for sufficiently low oxygen fractions and high helium fractions, $E_{\min}$ can fall below 2 MeV from helium band EMIC waves. Ross et al. (2021) showed that 80% of hydrogen band waves are in regions with densities less than average plasmaspheric values and therefore will infrequently interact with ~2 MeV electrons.

3. Wave Data

In this work, we made use of the hydrogen and helium band EMIC waves that were identified in Ross et al. (2021). The EMIC wave spectra were determined from the 64 Hz magnetometer data from the EMFISIS instrument (Kletzing et al., 2013) on board Van Allen Probe A over the duration of the mission (Mauk et al., 2013). Observations with no corresponding f_{pe}/f_{ce} measurement in the level 4 EMFISIS data were excluded (Kurth et al., 2015). For consistency with the other diffusion matrices presented in this study, we adopted the magnetic field model from Olson and Pfitzer (1977).

3.1. Constraining the Ion Composition

The uppermost frequency of the stop band of a given EMIC wave band is the asymptotic limit of the corresponding left-handed dispersion curve as k tends to zero (Figure 1a). It therefore introduces a low-frequency limit to the permissible frequency range, whereby no left-handed waves are allowed below it. As shown in Figure 1a, the ion composition affects the stop bands of hydrogen and helium band waves differently. Here we took a statistical approach and determined what proportion of the observed left-handed wave power is above the stop band, I_{stop}/I, for each wave band as a function of MLT and L^* for the three ion compositions. We first ensured that only left-handed waves were included by only considering waves with negative ellipticity. We then integrated the fitted Gaussian wave spectra for each observation from Ross et al. (2021) between the lower cutoff and upper cutoff determined from the observations to determine the wave intensity for each wave, I. We then summed over all observations in each 1 hr MLT and 0.5 L^* bin to obtain I. To calculate I_{stop}, the same procedure was performed but using the maximum of the stop band frequency and the observed lower cutoff as the integration minima.

The percentage of the wave intensity above the K14 stop band for hydrogen (Figure 2a) and helium (Figure 2b) band waves is uniform in MLT. If we sum over MLT and L^* before taking the ratio, then ~93.6% and ~98.8% of the wave power is above the stop band for H⁺ and He⁺ band EMIC waves, respectively. The low η_{He+} and η_{O+} fractions lead to a low-frequency stop band and therefore it imposes only a weak constraint on the frequency range of the EMIC waves of both types (Figure 1a). For M03, the wave intensity below the stop band is much larger for both bands, with only 8.4% of the wave intensity above the stop band for H⁺ band waves and 77.6% for He⁺ band waves. Most of the H⁺ wave intensity is inconsistent with M03, while the majority of the He⁺ wave intensity is consistent with it. There is a slight day-night asymmetry for H⁺ band waves (Figure 2c) with a lower proportion of wave power below the stop band on the day side. This coincides with in an increase in the average ratio between the central Gaussian frequency and the proton gyrofrequency, $<f_m/f_{cp}>$. The larger I_{stop}/I_I on the day-side at $L^* < 4.5$ mainly corresponds to times when $Dst < -20$ nT as few H⁺ band waves are observed in
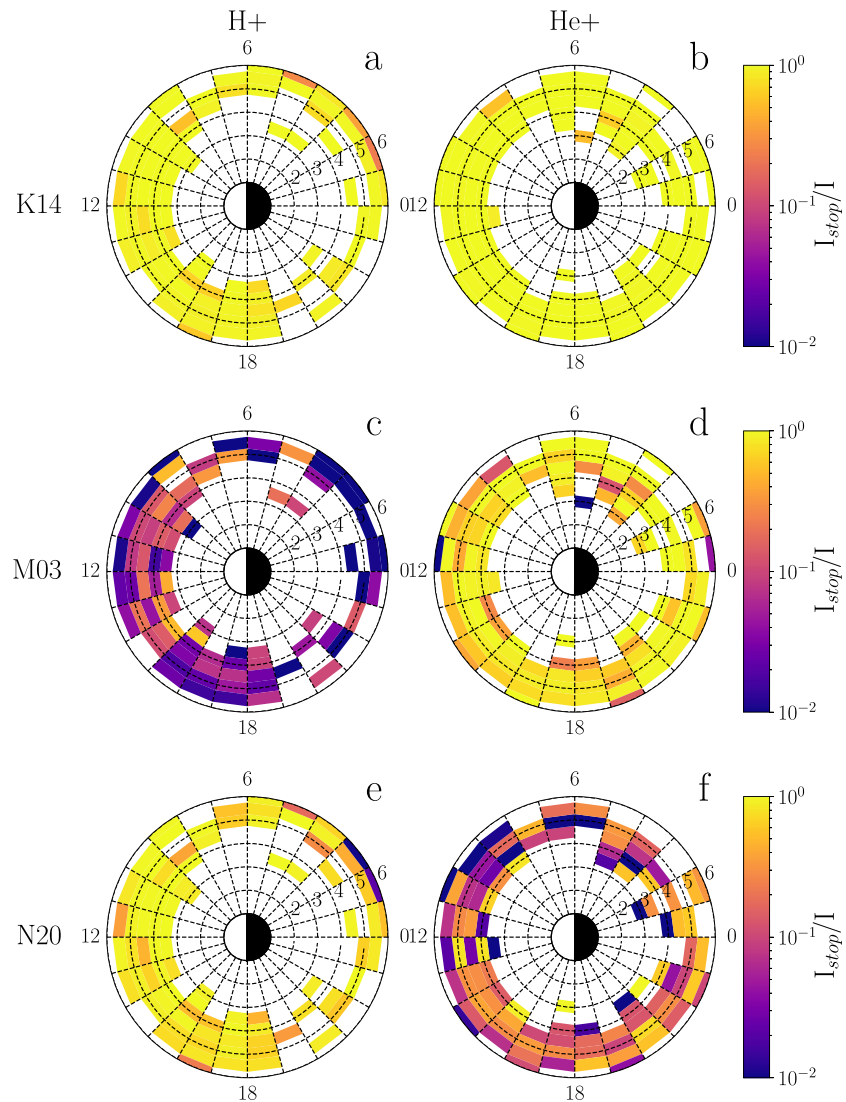
Figure 2. Panels (a) and (b) show the MLT and $L*$ dependence of the fraction of EMIC wave power above the stop band, assuming the K14 ion composition, for hydrogen and helium band waves, respectively. Panels (c) and (d) show the same but with the M03 ion composition, and panels (e) and (f) show the equivalent for the N20 ion composition.

this region when $Dst > -20$ nT. For N20, 83.5% of hydrogen band wave intensity lies above the hydrogen stop band while 22.6% of the helium band wave intensity is above the helium stop band. For the helium band waves, a higher proportion of wave power is consistent with N20 between 11 and 2 MLT (Figure 2f). This region coincides with larger EMIC occurrence rates (Ross et al., 2021). The high η_{O+} of N20 significantly raises the stop band of He$^+$ compared to K14 and M03, imposing a severe constraint on the permissible wave frequency range which is inconsistent with the majority of the observed wave intensity.

4. Global Simulations

Here, we investigate what effect ion composition has on the radiation belt population and the sensitivity of global radiation belt models to the composition. To model the radiation belt, we used the British Antarctic Survey Radiation Belt Model (BAS-RBM) (Glauert et al., 2014a, 2014b) which is based on the phase-averaged Fokker-Planck equation that calculates the evolution of the electron phase space density.

We considered a slow decay period following the geomagnetic storm in March 2015 when ultrarelativistic electrons were found at $L* \geq 3$. Van Allen Probes background corrected MagEIS electron flux (Blake et al., 2013;
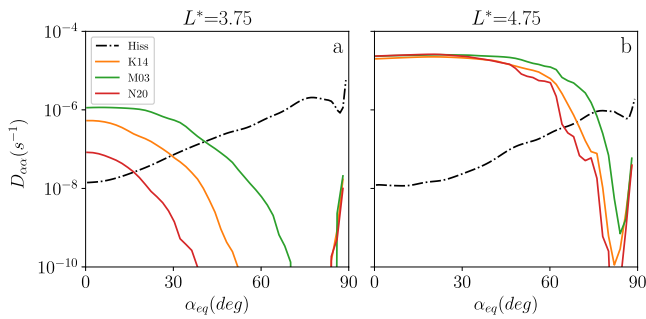
Figure 3. Bounce averaged diffusion coefficients for 4.2 MeV electrons at $L^* = 3.25$ (a) and $L^* = 4.75$ (b) with $-20\ nT \leq D\mathrm{st} < -10\ nT$. The diffusion coefficients curves are colored by the ion composition: K14 (orange), M03 (green), and N20 (red). For comparison, the hiss diffusion coefficients at $AE^* = 100$ nT are shown by the dash-dot curves.

Claudepierre et al., 2015) and REPT (Baker et al., 2013) electron flux were used for both the initial conditions and the boundary conditions at L_{min}, L_{max}, and E_{min}. The inner L^* boundary was set to 2.5 and the outer L^* boundary to 5.3. The minimum energy boundary was determined by assuming constant first adiabatic invariant with $E = 150$ keV at the outer L^* boundary. A zero flux gradient was used at the $\alpha_{eq} = 0°$ and $90°$ boundaries, while losses were included on the quarter bounce timescale inside the 100 km atm dipole loss cone. The chorus diffusion coefficients were parameterized by Kp (Meredith et al., 2020; Reidy et al., 2021) and the hiss diffusion coefficients were parameterized by AE (Allison et al., 2019; Meredith et al., 2018). The wave modes were separated by the Carpenter and Anderson (1992) plasmapause. The effects of EMIC waves are also included as diffusion coefficients which are explained in more detail in the next section. For radial diffusion, we used the Kp-driven magnetic component of the Brautigam and Albert (2000) formalism. The location of the last closed drift shell was accounted for following Glauert et al. (2014b).

4.1. EMIC Diffusion Coefficients

To include the effects of EMIC waves on radiation belt electrons in global radiation belt simulations, we calculated bounce and drift averaged electron diffusion coefficients following the approach from Ross et al. (2021). The diffusion coefficients were calculated in L^* (size 0.5 L^*) and Dst bins by averaging observation-specific diffusion coefficients from each concurrent wave spectra and plasma density measurement. Calculated in this way, a wide range of possible wave-particle interactions were included in the model unlike other statistical models that adopt one Gaussian spectrum and an L-dependent density (Kersten et al., 2014). The observation-specific bounce averaged diffusion coefficients were calculated using quasi-linear theory in the PADIE code (Glauert & Horne, 2005) which solves the cold plasma dispersion relation.

As noted in Section 3, the range of EMIC wave frequencies that are permissible is dependent on the ion composition. Therefore, any statistical model, which does not include knowledge of the ion composition during each individual EMIC observation, will have a degree of inconsistency for some of the observations. For instance, in the oxygen torus where the oxygen fraction is high, then the dispersion curve for helium band EMIC waves will be restricted to frequencies close to the helium gyrofrequency. However, the observations in the statistical model have come from regions with a range of different ion compositions, including those where waves are allowed, and observed, at lower frequencies than that permitted in the oxygen torus. In our diffusion coefficient calculations, these inconsistent ion composition-observation pairs do not contribute to the diffusion as there will be no corresponding EMIC dispersion curve. Therefore, the diffusion coefficients calculated using M03 omit the majority of hydrogen band wave power but retain nearly all of the helium band wave power. On the other hand, the diffusion coefficients calculated using N20 include most of the hydrogen band wave power but omit the majority of the helium band wave power. As over 90% of both the hydrogen and helium band wave intensity is consistent with the K14 ion composition, the majority of the wave power is included. As a result, our diffusion coefficients are conservative estimates but the omitted waves typically have low frequencies and high resonant energies and therefore are less important for radiation belt electrons of several MeV.

For 4.2 MeV electrons, the range of pitch-angles that are diffused by EMIC waves depends on the ion composition (Figure 3) and the range extends to larger α_{eq} for M03 (green) while the diffusion for N20 (red) is most tightly restricted to lower pitch-angles. At $L^* = 3.75$, the diffusion rates are also larger for M03 near the loss cone, that is, the diffusion of several MeV electrons into the loss cone is more effective at high helium fractions and is particularly ineffective in the oxygen torus. At $L^* = 4.75$, M03 still gives higher diffusion rates at $\alpha_{eq} \geq 30°$ but the rates near the loss cone are approximately equal for the three ion compositions. For comparison, the diffusion rates from hiss waves at $AE^* = 100$ nT inside the plasmasphere are shown by the black line. At $L^* = 3.75$, hiss waves dominate the diffusion at $\alpha_{eq} > 20°–45°$ while EMIC waves are more effective at lower pitch-angles. At $L^* = 4.75$, the diffusion rates from EMIC waves exceed those of hiss up to $\sim 60°–75°$ while hiss waves diffuse the electrons mirroring near the equator that are largely left alone by the EMIC waves. As the M03 diffusion coefficients extend to larger α_{eq} and the diffusion rate by hiss waves increases with α_{eq}, the minima in the diffusion
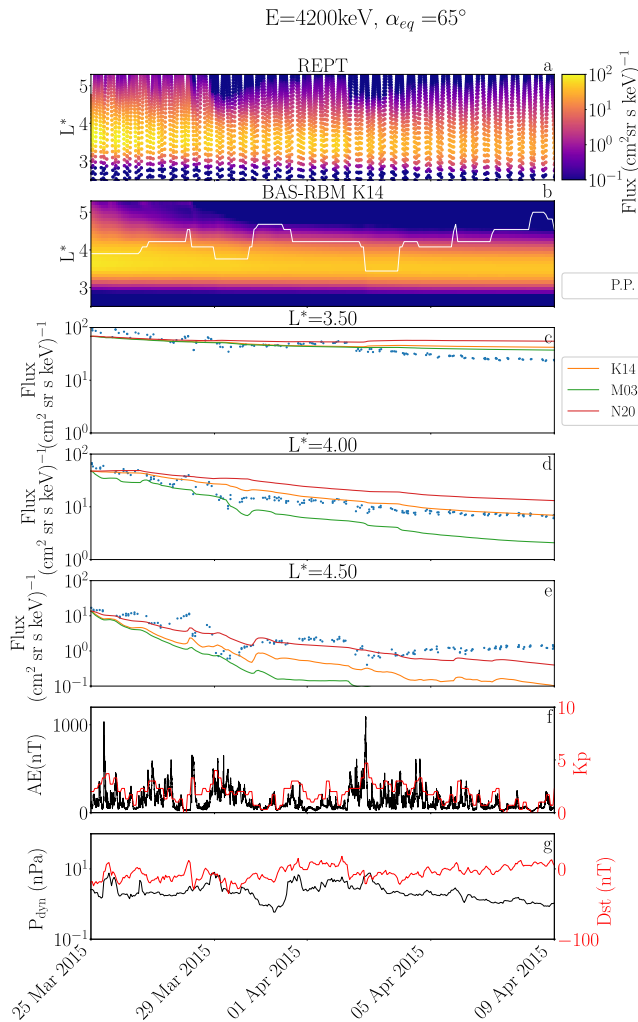
Figure 4. Panel (a) shows the $65 \pm 5°$ 4.2 MeV electron flux as measured by the two REPT instruments separately averaged over 5 min intervals. The pitch-angle has been mapped to the equator using OP77Q. Panel (b) shows flux as modeled by BAS-RBM using the K14 ion composition for the same pitch-angle and energy. Panels (c)–(e) show the REPT data in blue and modeled flux at $L^* = 3.5$, 4.0, and 4.5, respectively. For the VAP data, the tolerance is set to $\pm 0.025\ L^*$ and averaged at 5 min intervals.

rate across all α_{eq} at fixed energy are increased and consequently the effective diffusion bottleneck is reduced.

4.2. Results

Following March 17, 2015 storm with a minimum Dst of -223 nT, an ultra-relativistic electron belt was formed extending down to $L^* \sim 3$. Here we considered the steady decay that followed, once the ultrarelativistic belt was formed (Figure 4a). The last closed drift shell is well outside the model domain at $L^* \geq 6.5$ (calculated using TS04) during the interval, and hence we conclude that the effect of magnetopause shadowing is minimal. At $L^* \sim 3.5$ and $\alpha_{eq} = 65°$ (Figure 4c), all three simulations give very similar results until April 1, 2015 and are in good agreement with the observations, after which all three models overestimate the flux. The overestimation is likely due to too much radial diffusion on April 3rd when Kp temporally reaches 4.7. At larger L^*, the three ion compositions lead to significantly different behavior (Figures 4d and 4e). M03 (green line) has the fastest loss rates while N20 (red line) has the slowest, with the difference more pronounced at larger L^*. K14 is generally in good agreement with the data at $L^* = 4.0$, while at larger L^* the agreement is reasonable before April 1st but under predicts the flux later in the simulation, showing continual decay while the observations plateau. M03 significantly underestimates the flux after March 30th down to lower L^*, ~ 4, and at $L^* = 4.5$, the discrepancy is over an order of magnitude. At $L^* \geq 4.5$, there is an increase in the observed flux between March 29th which is not captured in the model (Figure 4a), this may partly explain the subsequent underestimate in flux at large L^*.

As shown in Figure 3, the EMIC diffusion coefficients are highly pitch-angle dependent, with those with the M03 ion composition extending to pitch-angles closer to 90° than for the K14 and N20 compositions. We therefore show in Figure 5 the evolution of the pitch-angle distribution at the heart of the belt during the event. The pitch-angle distributions from K14 (panel b) and N20 (panel d) are in strongest agreement with the REPT instruments (panel a), while M03 (panel c) leads to a narrower and faster decaying distribution. The pitch-angle distribution in the three models shows a repeated narrowing and broadening as a result of the combined action of EMIC and hiss waves. Before March 27th, $L^* = 4.0$ is slightly outside of the Carpenter and Anderson plasmapause (Figure 4b white line) and Kp is fairly low, therefore EMIC and low amplitude chorus waves are acting on the electron distribution leading to a fairly peaked distribution. The EMIC waves can effectively diffuse the electrons up to ~70° but are ineffective at larger α_{eq}, leaving a

peaked distribution. The plasmapause then moves outward, allowing hiss waves to diffuse the near 90° particles, flattening the distribution. Early on April 29th, the REPT data shows a fast decrease in flux and narrowing of the distribution. A similar feature is seen in the models but later in the day, resulting from the plasmapause moving inward. At this time, M03 shows too highly peaked a distribution while K14 and N20 are significantly broader.

5. Discussions

The heavy ion fraction strongly affects the banded structure of EMIC waves, imposing a low-frequency constraint on the frequency range of EMIC waves that can be present in any given band. Our findings indicate that the majority of H+ band EMIC wave power is consistent with low η_{He+} when using a cold plasma dispersion relation. In particular, if the storm time ion composition from Meredith et al. (2003) is adopted, then only ~8% of the wave power is above the stop band. While ~94% and ~84% of the wave power are consistent with the ion composition from Kersten et al. (2014) and the oxygen torus composition from Nosé et al. (2020), respectively. Similarly, linear growth rate calculations show that η_{He+} more strongly suppresses H+ band wave growth than η_{O+} (Nosé
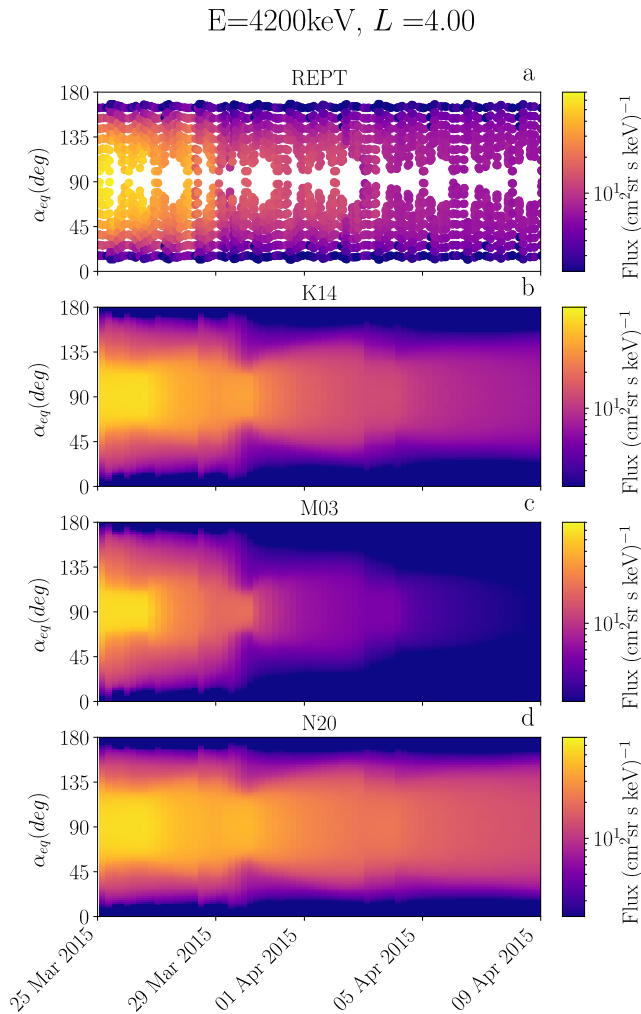
E=4200keV, L =4.00

Figure 5. Panel (a) shows the 4.2 MeV electron flux as a function of time and equatorial pitch-angle at $L^* = 4.0$. The local pitch-angles have been mapped to the equator using OP77Q. The values are averaged over 5 min intervals for each satellite and within a tolerance of $L^* \pm 0.025$. Panels (b)–(d) show the pitch-angle dependent flux in simulations K14, M03, and N20.

et al., 2020). On the other hand, high η_{He+}, such as Meredith et al. (2003), does not impose such a tight constraint on He+ band EMIC waves, and is consistent with ~78% of the wave power. Contrastingly, only 23% of the He+ band EMIC wave power is consistent with the oxygen torus model from Nosé et al. (2020), suggesting that little of the He+ wave power is inside the oxygen torus. In fact, the theoretical calculations show that the linear growth rates of He+ band EMIC waves are reduced inside the oxygen torus (Min et al., 2015). We find an MLT asymmetry in the fraction of helium band wave power above the stop band with an increased fraction above the stop band between 11 and 2 MLT. The oxygen tori have been found over all MLT (Roberts et al., 1987). Again, the ion composition from Kersten et al. (2014) is consistent with the vast majority of He+ EMIC band observations, with ~98% of wave power above the stop band.

The cold ion composition affects the resonant interactions between EMIC waves and radiation belt electrons. A high hydrogen fraction decreases the energies of the electrons that resonate with a hydrogen band EMIC wave, while a high helium content reduces the electron resonant energies for helium band waves. As a result, increasing the fraction of an ion species leads to more EMIC waves of the corresponding band being able to resonate with several MeV radiation belt electrons. Increasing the helium fraction and reducing the hydrogen fraction will decrease the resonant energy of helium band waves but increase the resonant energies of hydrogen band. The net effect on the diffusion of MeV electrons is determined by these competing effects. In statistical diffusion coefficients calculated by including the distribution of wave spectra and plasma density for both bands, as done here, we find that increasing the helium fraction leads to increased diffusion rates of several MeV electrons, that is, the increased diffusion rate from helium band waves dominates over the decreased diffusion rate form hydrogen band waves. More helium band EMIC waves are able to resonate with several MeV electrons than hydrogen band waves (Ross et al., 2021), resulting in the higher sensitivity to helium fraction. This is partly due to the larger population of helium band waves in high-density regions, such as the plasma plumes, which reduces the resonant energies.

For global simulations of the decay of the ultrarelativistic electron, the best agreement between the decay of 4.2 MeV electrons observed by REPT and BAS-RBM is found when the helium fraction is low (Figures 4 and 5). We also note that EMIC diffusion coefficients with a helium fraction of 20% significantly over estimate the loss rates, particularly at $L^* = 4 - 5$, when coincident measurements of wave frequency and plasma density are included. This suggests that the storm time estimate from ion composition from Meredith et al. (2003) may not always be appropriate.

Ross et al. (2020) showed that including the variation in EMIC wave spectra and plasma density significantly improves the agreement between global models and observations of 2–4 MeV electrons, when compared to modules using average plasma density and wave spectra. Similar conclusions on the importance of plasma density have been drawn by Shprits et al. (2022). Despite this, previous studies using average density models, a representative but not average, helium band wave spectra and a fixed assumed ion composition have been found to well reproduce the behavior of EMIC waves in the radiation belts (Drozdov et al., 2017; Ma et al., 2015). However, as shown here, the ion composition affects the decay rate significantly and therefore should be considered when modeling the decay of the relativistic and ultrarelativistic electron flux. For instance, the slowest decay is found using the oxygen torus ion composition from Nosé et al. (2020) suggesting that an oxygen torus may suppress the decay of the ultrarelativistic storage ring by hydrogen and helium band EMIC waves. The next step will require accurate measurements of the cold ion composition during EMIC wave observations, such that models include consistent ion compositions, plasma densities, and wave properties. The transport of ions into the inner magnetosphere is increased during storms and substorms. However, there is no consensus on whether the average ion mass

increases or decreases during enhanced geomagnetic activity. For instance, some studies have found decreases in the average ion mass (Dent et al., 2006; Menk et al., 2014), while others have found increases (Kronberg et al., 2014; Wharton et al., 2020). Similarly, we found no distinguishable dependence on Dst in the percentage of wave power above the stop band for any of the ion compositions considered here. The oxygen ion fraction has been found to vary across the plasmapause (Grew et al., 2007) further complicating the inclusion in global radiation belt models (Wang et al., 2014). The intensity of O^+ ionospheric outflows is dependent on solar activity and changes with the solar cycle through the effect of EUV radiation on ionospheric properties (Yau et al., 1985). Similarly, ion composition in the plasma sheet is correlated with solar activity (F10.7) (Lennartsson, 1989; Young et al., 1982). As a result, it may be necessary to include solar cycle dependence of ion compositions in radiation belt simulations multi-year radiation belt simulations.

6. Conclusions

In this paper, we have explored the effects of widely varying ion compositions on the decay of ultra-relativistic electrons in the Earth's radiation belts. We considered three models, two with similar He^+ compositions but very different O^+ compositions, and one with high He^+ and O^+ compositions. Our main conclusions are:

1. We find that over 90% of the hydrogen and helium band EMIC wave intensity is consistent with a cold helium and oxygen ion composition of a few percent. In comparison, 10% of hydrogen band EMIC wave intensity is consistent with a high helium composition of 20%, and only a similar small percentage of helium wave intensity is consistent with an oxygen torus ion composition.
2. The ion composition affects the resonant energy of EMIC waves leading to significantly different decay rates. As a result, the decay of ultrarelativistic (4.2 MeV) electrons in the storage ring is sensitive to the ion composition.
3. Large He^+ concentrations lead to decay rates that are too fast. We find better agreement between the Van Allen Probe observations and a global radiation belt model when the He^+ composition is low, typically only a few percent, compared to higher values in the region of 20%. This is for a wide range of O^+ from 1% to 16%.

Modeling the decay of the radiation belts remains a difficult problem, compounded by the problem of measuring the thermal heavy ion composition which is very difficult to do using spacecraft. Nevertheless, we suggest that more observations from both ground and space, especially during the formation of the oxygen ion torus after a geomagnetic storm, would help understand and set constraints on the decay of ultra-relativistic electrons in the radiation belts.

Data Availability Statement

The EMIC diffusion coefficients calculated here can be downloaded from the UK Polar Data Centre at https://doi.org/10.5285/2ba39ec4-c89e-4091-bdf9-e40491ec92a5.

References

Albert, J. M. (2003). Evaluation of quasi-linear diffusion coefficients for emic waves in a multispecies plasma. *Journal of Geophysical Research*, *108*, 1249. https://doi.org/10.1029/2002JA009792

Allison, H. J., Horne, R. B., Glauert, S. A., & Zanna, G. D. (2019). On the importance of gradients in the low-energy electron phase space density for relativistic electron acceleration. *Journal of Geophysical Research: Space Physics*, *124*, 2628–2642. https://doi.org/10.1029/2019JA026516

André, M., & Cully, C. M. (2012). Low-energy ions: A previously hidden solar system particle population. *Geophysical Research Letters*, *39*, L03101. https://doi.org/10.1029/2011GL050242

Baker, D. N., Kanekal, S. G., Hoxie, V. C., Henderson, M. G., Li, X., Spence, H. E., et al. (2013). A long-lived relativistic electron storage ring embedded in Earth's outer Van Allen belt. *Science*, *340*, 186. http://science.sciencemag.org/content/340/6129/186.abstract

Blake, J. B., Carranza, P. A., Claudepierre, S. G., Clemmons, J. H., Crain, W. R., Dotan, Y., et al. (2013). The magnetic electron ion spectrometer (MagEIS) instruments aboard the radiation belt storm probes (RBSP) spacecraft. *Space Science Reviews*, *179*, 383–421. https://doi.org/10.1007/s11214-013-9991-8

Brautigam, D. H., & Albert, J. M. (2000). Radial diffusion analysis of outer radiation belt electrons during the October 9, 1990, magnetic storm. *Journal of Geophysical Research*, *105*, 291–309. https://doi.org/10.1029/1999ja900344

Cao, X., Shprits, Y. Y., Ni, B., & Zhelavskaya, I. S. (2017). Scattering of ultra-relativistic electrons in the Van Allen radiation belts accounting for hot plasma effects. *Scientific Reports*, *7*, 17719. https://doi.org/10.1038/s41598-017-17739-7

Carpenter, D. L., & Anderson, R. R. (1992). An ISEE/whistler model of equatorial electron density in the magnetosphere. *Journal of Geophysical Research*, *97*, 1097. https://doi.org/10.1029/91ja01548

Chappell, C. R. (1988). 'The terrestrial plasma source' a new perspective in solar-terrestrial processes from dynamics explorer. *Reviews of Geophysics*, *26*, 229–248. https://doi.org/10.1029/rg026i002p00229

Claudepierre, S. G., O'Brien, T. P., Blake, J. B., Fennell, J. F., Roeder, J. L., Clemmons, J. H., et al. (2015). A background correction algorithm for Van Allen probes mageis electron flux measurements. *Journal of Geophysical Research - A: Space Physics*, *120*, 5703–5727. https://doi.org/10.1002/2015JA021171

Comfort, R. H., Newberry, I. T., & Chappell, C. R. (1988). *Preliminary statistical survey of plasmaspheric ion properties from observations by de 1/rims*. https://doi.org/10.1029/GM044p0107

Dent, Z. C., Mann, I. R., Goldstein, J., Menk, F. W., & Ozeke, L. G. (2006). Plasmaspheric depletion, refilling, and plasmapause dynamics: A coordinated ground-based and image satellite study. *Journal of Geophysical Research*, *111*, A03205. https://doi.org/10.1029/2005JA011046

Denton, R. E., Jordanova, V. K., & Bortnik, J. (2015). Resonance of relativistic electrons with electromagnetic ion cyclotron waves. *Geophysical Research Letters*, *42*, 8263–8270. https://doi.org/10.1002/2015GL064379

Drozdov, A. Y., Shprits, Y. Y., Usanova, M. E., Aseev, N. A., Kellerman, A. C., & Zhu, H. (2017). Emic wave parameterization in the long-term verb code simulation. *Journal of Geophysical Research: Space Physics*, *122*, 8488–8501. https://doi.org/10.1002/2017JA024389

Glauert, S. A., & Horne, R. B. (2005). Calculation of pitch angle and energy diffusion coefficients with the PADIE code. *Journal of Geophysical Research*, *110*, A04206. https://doi.org/10.1029/2004JA010851

Glauert, S. A., Horne, R. B., & Meredith, N. P. (2014a). Simulating the Earth's radiation belts: Internal acceleration and continuous losses to the magnetopause. *Journal of Geophysical Research: Space Physics*, *119*, 7444–7463. https://doi.org/10.1002/2014JA020092

Glauert, S. A., Horne, R. B., & Meredith, N. P. (2014b). Three-dimensional electron radiation belt simulations using the bas radiation belt model with new diffusion models for chorus, plasmaspheric hiss, and lightning-generated whistlers. *Journal of Geophysical Research: Space Physics*, *119*, 268–289. https://doi.org/10.1002/2013JA019281

Grew, R. S., Menk, F. W., Clilverd, M. A., & Sandel, B. R. (2007). Mass and electron densities in the inner magnetosphere during a prolonged disturbed interval. *Geophysical Research Letters*, *34*, L02108. https://doi.org/10.1029/2006GL028254

Horwitz, J. L. (1984). Features of ion trajectories in tile polar magnetosphere. *Geophysical Research Letters*, *11*, 1111–1114. https://doi.org/10.1029/gl011i011p01111

Kersten, T., Horne, R. B., Glauert, S. A., Meredith, N. P., Fraser, B. J., & Grew, R. S. (2014). Electron losses from the radiation belts caused by EMIC waves. *Journal of Geophysical Research: Space Physics*, *119*, 8820–8837. https://doi.org/10.1002/2014JA020366

Kletzing, C. A., Kurth, W. S., Acuna, M., MacDowall, R. J., Torbert, R. B., Averkamp, T., et al. (2013). The electric and magnetic field instrument suite and integrated science (EMFISIS) on RBSP. *Space Science Reviews*, *179*, 127–181. https://doi.org/10.1007/s11214-013-9993-6

Kronberg, E. A., Ashour-Abdalla, M., Dandouras, I., Delcourt, D. C., Grigorenko, E. E., Kistler, L. M., et al. (2014). *Circulation of heavy ions and their dynamical effects in the magnetosphere: Recent observations and models* (Vol. 184). Kluwer Academic Publishers. https://doi.org/10.1007/s11214-014-0104-0

Kurth, W. S., Pascuale, S. D., Faden, J. B., Kletzing, C. A., Hospodarsky, G. B., Thaller, S., & Wygant, J. R. (2015). Electron densities inferred from plasma wave spectra obtained by the waves instrument on Van Allen probes. *Journal of Geophysical Research: Space Physics*, *120*, 904–914. https://doi.org/10.1002/2014JA020857

Lee, J. H., & Angelopoulos, V. (2014). On the presence and properties of cold ions near earth's equatorial magnetosphere. *Journal of Geophysical Research: Space Physics*, *119*, 1749–1770. https://doi.org/10.1002/2013JA019305

Lee, J. H., Blum, L. W., & Chen, L. (2021). On the impacts of ions of ionospheric origin and their composition on magnetospheric EMIC waves. *Frontiers Media S.A.*, *8*. https://doi.org/10.3389/fspas.2021.719715

Lennartsson, W. (1989). Energetic (0.1- to 16-kev/e) magnetospheric ion composition at different levels of solar f 10.7. *Journal of Geophysical Research*, *94*, 3600. https://doi.org/10.1029/ja094ia04p03600

Ma, Q., Li, W., Thorne, R. M., Ni, B., Kletzing, C. A., Kurth, W. S., et al. (2015). Modeling inward diffusion and slow decay of energetic electrons in the Earth's outer radiation belt. *Geophysical Research Letters*, *42*, 987–995. https://doi.org/10.1002/2014GL062977

Mauk, B. H., Fox, N. J., Kanekal, S. G., Kessel, R. L., Sibeck, D. G., & Ukhorskiy, A. (2013). Science objectives and rationale for the radiation belt storm probes mission. *Space Science Reviews*, *179*, 3–27. https://doi.org/10.1007/s11214-012-9908-y

Menk, F., Kale, Z., Sciffer, M., Robinson, P., Waters, C., Grew, R., et al. (2014). Remote sensing the plasmasphere, plasmapause, plumes and other features using ground-based magnetometers. *Journal of Space Weather and Space Climate*, *4*, A34. https://doi.org/10.1051/swsc/2014030

Meredith, N. P., Horne, R. B., Kersten, T., Li, W., Bortnik, J., Sicard, A., & Yearby, K. H. (2018). Global model of plasmaspheric hiss from multiple satellite observations. *Journal of Geophysical Research: Space Physics*, *123*, 4526–4541. https://doi.org/10.1029/2018JA025226

Meredith, N. P., Horne, R. B., Shen, X. C., Li, W., & Bortnik, J. (2020). Global model of whistler mode chorus in the near-equatorial region (||λm| < 18°). *Geophysical Research Letters*, *47*, e2020GL087311. https://doi.org/10.1029/2020GL087311

Meredith, N. P., Thorne, R. M., Horne, R. B., Summers, D., Fraser, B. J., & Anderson, R. R. (2003). Statistical analysis of relativistic electron energies for cyclotron resonance with EMIC waves observed on CRRES. *Journal of Geophysical Research*, *108*, 1250. https://doi.org/10.1029/2002JA009700

Min, K., Liu, K., Bonnell, J. W., Breneman, A. W., Denton, R. E., Funsten, H. O., et al. (2015). Study of emic wave excitation using direct ion measurements. *Journal of Geophysical Research: Space Physics*, *120*, 2702–2719. https://doi.org/10.1002/2014JA020717

Miyoshi, Y., Sakaguchi, K., Shiokawa, K., Evans, D., Albert, J., Connors, M., & Jordanova, V. (2008). Precipitation of radiation belt electrons by EMIC waves, observed from ground and space. *Geophysical Research Letters*, *35*, L23101. https://doi.org/10.1029/2008GL035727

Nosé, M., Matsuoka, A., Kumamoto, A., Kasahara, Y., Teramoto, M., Kurita, S., et al. (2020). Oxygen torus and its coincidence with EMIC wave in the deep inner magnetosphere: Van Allen probe B and Arase observations. *Earth Planets and Space*, *72*, 111. https://doi.org/10.1186/s40623-020-01235-w

Olsen, R. C., Chappell, C. R., Gallagher, D. L., Green, J. L., & Gurnett, D. A. (1985). The hidden ion population: Revisited. *Journal of Geophysical Research*, *90*, 12121. https://doi.org/10.1029/ja090ia12p12121

Olson, W. P., & Pfitzer, K. A. (1977). Magnetospheric magnetic field modeling. Annual scientific report. Retrieved from https://www.osti.gov/biblio/7212748

Reidy, J. A., Horne, R. B., Glauert, S. A., Clilverd, M. A., Meredith, N. P., Woodfield, E. E., et al. (2021). Comparing electron precipitation fluxes calculated from pitch angle diffusion coefficients to Leo satellite observations. *Journal of Geophysical Research: Space Physics*, *126*, e2020JA028410. https://doi.org/10.1029/2020JA028410

Roberts, W. T., Horwitz, J. L., Comfort, R. H., Chappell, C. R., Waite, J. H., & Green, J. L. (1987). Heavy ion density enhancements in the outer plasmasphere. *Journal of Geophysical Research*, *92*, 13499. https://doi.org/10.1029/ja092ia12p13499

Rodger, C. J., Raita, T., Clilverd, M. A., Seppälä, A., Dietrich, S., Thomson, N. R., & Ulich, T. (2008). Observations of relativistic electron precipitation from the radiation belts driven by EMIC waves. *Geophysical Research Letters*, *35*, L16106. https://doi.org/10.1029/2008GL034804

Ross, J. P. J., Glauert, S. A., Horne, R. B., Watt, C. E., Meredith, N. P., & Woodfield, E. E. (2020). A new approach to constructing models of electron diffusion by EMIC waves in the radiation belts. *Geophysical Research Letters*, *47*, e2020GL088976. https://doi.org/10.1029/2020GL088976

Ross, J. P. J., Glauert, S. A., Horne, R. B., Watt, C. E. J., & Meredith, N. P. (2021). On the variability of emic waves and the consequences for the relativistic electron radiation belt population. *Journal of Geophysical Research: Space Physics*, *126*(12), e2021JA029754. https://doi.org/10.1029/2021JA029754

Shprits, Y. Y., Allison, H. J., Wang, D., Drozdov, A., Szabo-Roberts, M., Zhelavskaya, I., & Vasile, R. (2022). A new population of ultra-relativistic electrons in the outer radiation zone. *Journal of Geophysical Research: Space Physics*, *127*, e2021JA030214. https://doi.org/10.1029/2021ja030214

Shprits, Y. Y., Drozdov, A. Y., Spasojevic, M., Kellerman, A. C., Usanova, M. E., Engebretson, M. J., et al. (2016). Wave-induced loss of ultra-relativistic electrons in the Van Allen radiation belts. *Nature Communications*, *7*, 12883. https://doi.org/10.1038/ncomms12883

Shprits, Y. Y., Kellerman, A., Aseev, N., Drozdov, A. Y., & Michaelis, I. (2017). Multi-MeV electron loss in the heart of the radiation belts. *Geophysical Research Letters*, *44*, 1204–1209. https://doi.org/10.1002/2016GL072258

Summers, D., & Thorne, R. M. (2003). Relativistic electron pitch-angle scattering by electromagnetic ion cyclotron waves during geomagnetic storm. *Journal of Geophysical Research*, *108*, 1143. https://doi.org/10.1029/2002JA009489

Thorne, R. M., & Kennel, C. F. (1971). Relativistic electron precipitation during magnetic storm main phase. *Journal of Geophysical Research*, *76*, 4446–4453. https://doi.org/10.1029/ja076i019p04446

Usanova, M. E., Drozdov, A., Orlova, K., Mann, I. R., Shprits, Y., Robertson, M. T., et al. (2014). Effect of emic waves on relativistic and ultra-relativistic electron populations: Ground-based and Van Allen probes observations. *Geophysical Research Letters*, *41*, 1375–1381. https://doi.org/10.1002/2013GL059024

Wang, D. D., Yuan, Z. G., Deng, X. H., Zhou, M., Huang, S. Y., Li, M., et al. (2014). Compression-related emic waves drive relativistic electron precipitation. *Science China Technological Sciences*, *57*, 2418–2425. https://doi.org/10.1007/s11431-014-5701-3

Watt, C. E., Allison, H. J., Meredith, N. P., Thompson, R. L., Bentley, S. N., Rae, I. J., et al. (2019). Variability of quasilinear diffusion coefficients for plasmaspheric hiss. *Journal of Geophysical Research: Space Physics*, *124*, 8488–8506. https://doi.org/10.1029/2018JA026401

Wharton, S. J., Rae, I. J., Sandhu, J. K., Walach, M. T., Wright, D. M., & Yeoman, T. K. (2020). The changing eigenfrequency continuum during geomagnetic storms: Implications for plasma mass dynamics and ULF wave coupling. *Journal of Geophysical Research: Space Physics*, *125*, e2019JA027648. https://doi.org/10.1029/2019JA027648

Yau, A. W., Beckwith, P. H., Peterson, W. K., & Shelley, E. G. (1985). Long-term (solar cycle) and seasonal variations of upflowing ionospheric ion events at de 1 altitudes. *Journal of Geophysical Research*, *90*, 6395. https://doi.org/10.1029/ja090ia07p06395

Young, D. T., Balsiger, H., & Geiss, J. (1982). Correlations of magnetospheric ion composition with geomagnetic and solar activity. *Journal of Geophysical Research*, *87*, 9077–9096. https://doi.org/10.1029/JA087iA11p09077

Yuan, Z., Liu, K., Yu, X., Yao, F., Huang, S., Wang, D., & Ouyang, Z. (2018). Precipitation of radiation belt electrons by emic waves with conjugated observations of NOAA and Van Allen satellites. *Geophysical Research Letters*, *45*, 12694–12702. https://doi.org/10.1029/2018GL080481